REPORT DOCUMENTATION PAGE

Form Approved
OMB No. 0704-0188

1. REPORT DATE *(DD-MM-YYYY)* 30-11-2009	2. REPORT TYPE Final Performance Report	3. DATES COVERED *(From - To)* 1 Dec 2006 – 30 Nov 2009
4. TITLE AND SUBTITLE **PRACTICAL E-BEAM GENERATION OF AIR PLASMA FOR AIRBORNE APPLICATIONS**		**5a. CONTRACT NUMBER**
		5b. GRANT NUMBER FA9550-07-1-0021
		5c. PROGRAM ELEMENT NUMBER
6. AUTHOR(S) Robert J Vidmar		**5d. PROJECT NUMBER**
		5e. TASK NUMBER
		5f. WORK UNIT NUMBER
7. PERFORMING ORGANIZATION NAME(S) AND ADDRESS(ES) University of Nevada, Reno Sponsored Projects, Mail Stop 325 1664 N Virginia Street Reno, NV 89557-0240		**8. PERFORMING ORGANIZATION REPORT NUMBER**
9. SPONSORING / MONITORING AGENCY NAME(S) AND ADDRESS(ES) AF Office of Scientific Research 875 N. Randolph St, Room 3112 Arlington, VA 22203		**10. SPONSOR/MONITOR'S ACRONYM(S)** AFOSR/NE
		11. SPONSOR/MONITOR'S REPORT NUMBER(S) AFRL-OSR-VA-TR-2012-0606

12. DISTRIBUTION / AVAILABILITY STATEMENT
UNLIMITED-A

13. SUPPLEMENTARY NOTES

14. ABSTRACT

   The generation and sustainment of air plasma generated by a high-energy electron beam and a sustaining electric field was investigated theoretically and experimentally. Theoretical calculations of power quantify a factor of 2 reduction in power at 60 Torr for a sustaining electric field of 0.4 Td. The reduction in power occurs because the detachment rate of electrons from negative oxygen ions is high and more efficient than generating free electrons via impact ionization. Experimentally, a 100 keV electron beam, operating with a few mA of beam current, ionized air in a 400-liter test cell with pressure ranging from 1 mTorr to 638 Torr. Optical measurements quantified the electron density profile along an RF propagation path. A microwave detection system measured the magnitude and phase of a RF signal at 10 GHz. The relative magnitude and phase of the RF signal quantify the complex wavenumber and permit calculation of the electron density and momentum-transfer collision rate. Measurements in the presence of a sustaining electric field indicated an influence on the electron density. The initial result is encouraging but difficult to interpret due to experimental details.

15. SUBJECT TERMS
Air Chemistry, Air Plasma, Electron Beam, E/N, I/Q Detector, Microwave, Plasma, Power,

16. SECURITY CLASSIFICATION OF: **UNCLASSIFIED**			17. LIMITATION OF ABSTRACT	18. NUMBER OF PAGES	19a. NAME OF RESPONSIBLE PERSON Robert J Vidmar
a. REPORT UNCLASSIFIED	**b. ABSTRACT** UNCLASSIFIED	**c. THIS PAGE** UNCLASSIFIED	UNCLASSIFIED UNLIMITED	32	**19b. TELEPHONE NUMBER** *(include area code)* 775 682-9742

Standard Form 298 (Rev. 8-98)
Prescribed by ANSI Std. Z39.18

PRACTICAL E-BEAM GENERATION OF AIR PLASMA FOR AIRBORNE APPLICATIONS

By: ROBERT J VIDMAR

Prepared for:

University of Nevada, Reno
1664 North Virginia Street
Reno, Nevada 89557-0240 USA

ABSTRACT

The generation and sustainment of air plasma generated by a high-energy electron beam and a sustaining electric field was investigated theoretically and experimentally. Theoretical calculations of power quantify a factor of 2 reduction in power at 60 Torr for a sustaining electric field of 0.4 Td. The reduction in power occurs because the detachment rate of electrons from negative oxygen ions is high and more efficient than generating free electrons via impact ionization. Experimentally, a 100 keV electron beam, operating with a few mA of beam current, ionized air in a 400-liter test cell with pressure ranging from 1 mTorr to 638 Torr. Optical measurements quantified the electron density profile along an RF propagation path. A microwave detection system measured the magnitude and phase of a RF signal at 10 GHz. The relative magnitude and phase of the RF signal quantify the complex wavenumber and permit calculation of the electron density and momentum-transfer collision rate. Measurements in the presence of a sustaining electric field indicated an influence on the electron density. The initial result is encouraging but difficult to interpret due to experimental details.

CONTENTS

FIGURES

TABLES

I INTRODUCTION

The underlying theme of the research conducted is to quantify a practical means of generating and sustaining plasma for airborne applications. For airborne applications the overall power budget to generate and sustain plasma directly relates to provisioning, energy consumption, heat dissipation, and overall feasibility. A high-energy electron beam is an efficient means of generating volumetric plasma and generates an electron-ion pair at a cost of 33.7 eV from the electron beam. Because electron generation, acceleration, and transmission through a foil window into air are efficient and well understood and have a net efficiency of approximately 75%, a single electron-ion pair requires approximately 45 eV from the AC mains. This energy is substantially lower than optical ionization that suffers from inefficient photon sources. Other approaches based on discharges require higher power and electrodes that extend into the plasma generation region. Electron beams do not require any external electrodes, have a maximum range determined by the air pressure and beam energy, and generate an axial electric field.

Application of a reduced electric field of approximately 0.4 Td (4×10^{-18} V-cm^2) is computationally shown to reduce the power to sustain a constant electron density by a factor of 2. The reduction by a factor of 2 occurs at 0.4 Td because the detachment rate of electrons from O_2^- is more efficient than generating free electrons via high-energy impact ionization. Above 0.4 Td electrons, electrons recombine and attach more quickly than they detach and the power increases. The axial electric field of the electron beam provides the reduced field and is tunable. For a repetitively pulsed system, reducing the duty ratio of the beam increases beam current and increases the axial electric field. The electron density relaxes between pulses, which increases the oxygen negative ions. Subsequent pulses increase the electron density, as detachment from the negative oxygen ions become more important. The axial electric field effectively recycles electrons from O_2^- via detachment driven by a reduced field of 0.4 Td.

An experiment using a grid system in the air-plasma test cell demonstrates this concept. The initial result is encouraging but difficult to interpret due to experimental details. A second-generation grid system and a more advanced E/N measurement system would clarify the current results.

II TECHNICAL APPROACH

A. <u>Electron-Beam Air-Plasma Apparatus</u>

The air-plasma test cell and electron beam system utilized for this project is shown in Fig. 1a. The air plasma test cell has an inside diameter of 36 in and an inside height of 24 in. The electron-beam source shown in Fig. 1a appears above the test cell and fires downward along the centerline of the test cell. A 0.5-mil aluminum transmission window, shown in Fig 1b, separates the vacuum for electron beam production from pressures ranging from 1 mTorr to 638 Torr in the test cell. A 10-mm thick honeycomb disk with 6.8 mm cells was bolted between two aluminum rings to provide a support for the transmission window from pressure loading from the test cell. The honeycomb support and transmission window bolt to the bottom side of the upper flange in Fig. 1a and Fig. 2. The honeycomb pattern is visible in Fig. 1b.

Approximately 100 lb of lead shielding encircle the electron beam source from the upper flange to the top of the electron beam source. The shielding reduces the continuous x-ray emission from the source at 100 keV to approximately the background radiation level. Additional x-ray emission information on this source and the volumetric ionization produced by it is in a final report for Contract FA9550-05-1-0087.

The electron beam source from Kimball Physics operates at 100 kV and produces up to 20 mA of beam current. The source can operate in either a pulsed or a continuous mode. Pulsed operation with 7-ms pulses and a 5-min repetition rate provided hundreds of pulses of nearly identical beam current. Addition of a 4.5-in CF cross and turbo pump, not shown in Fig. 1, between the source and transmission window increased the shot-to-shot beam current and overall reliability. The additional pumping from a 4.5-in turbo pump reduced the back streaming of gas from the transmission window region through a transit tube into the acceleration region of the electron-beam source. A systematic reduction of beam current of approximately 30% occurs after several hours of operation and correlates to a systematic increase of pressure in both the source and the transmission-window region.

A mesh current sensor monitored the beam current incident on the transmission window foil during a pulse. This sensor, shown in Fig. 1c, is a nickel mesh with 98% transmission.   It intercepts 2% of the beam current and connects to an oscilloscope through a matching network. This network produces a 1 V signal on the oscilloscope that corresponds to 1 mA of incident beam current. A sketch of the apparatus in Fig. 2 shows the major components and there relative orientation.   The mesh sensor is upstream of the transmission window and only provides the incident beam current on the honeycomb support and aluminum transmission window. A computational tool called MAGIC from ATK Mission Research models beam-current propagation through the foil and subsequent propagation into the air-plasma test cell. Code calculations provide beam-current profiles as a function of distance into the test cell and quantify a 15% energy loss of beam electrons emerging from the transmission window.
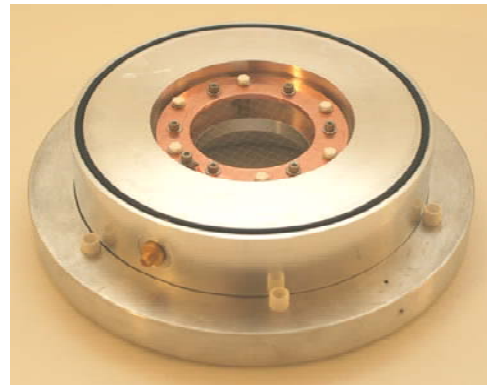
Figure 1. Air-plasma apparatus. a) Test cell and electron-beam source.
b) Atmospheric pressure loading of ½ mil aluminum transmission window.
c) Beam current mesh sensor.

Beam electrons propagate into the test cell and the beam diameter expands. This is due to a beam divergence associated with scattering in the transmission window foil and space charge spreading. Simulations with MAGIC as a function of pressure in the test cell region indicate scattering in the foil is the dominant cause of beam expansion at low pressure. Because all the diagnostics in Fig. 2 are located with centerlines 12-in from the bottom of the test cell, the diagnostics all made measurements on the midplane of the test cell.

An in-phase and quadrature (I/Q) microwave diagnostic system at 10 GHz provides for measurement of the chord averaged electron number density and the chord averaged momentum-transfer collision rate. An optical system quantifies the electron density profile along the microwave transmission path. The photograph in Fig. 3 shows the general layout of these diagnostics. The 8-in CF nipples on the outside of the test cell house the RF horns. The tip of the receive horn is visible on the right side of the tank in Fig. 3. The transmit horn is slightly recessed from the hole in the white RF

ALUMINUM HONEYCOMB
SUPPORT: ALLOY 5052

ALUMINUM TRANSMISSION
WINDOW: ALLOY 1145/1235-H19
12 μm (0.5 mil)

NICKEL MESH
98% TRANSMISSION

8X UV
OPTICAL
FIBERS

MESH
CURRENT
SENSOR

UV
OPTICAL
FIBER

INCIDENT
ELECTRONS
~ 100 keV

VACUUM FOR ELECTRON BEAM
8 X 10^{-10} Torr to 1 X 10^{-9} Torr

4.5-in CF
TURBO PUMP

APERTURE PLATE
60-mm ID

PRESSURE IN TEST CELL
638 Torr (LABORATORY)
150 Torr (30,000 ft)
1 mTorr (300,000 ft)

$\dfrac{dE}{ds_{foil}}$

BSE

SE

SE

ALUMINUM HOUSING
WITH 2% NICKEL MESH
ON CERAMIC STANDOFFS

CLAMPING RING

ENERGY DEPOSITION
OPTICAL EXCITATION OF AIR

$\dfrac{dE}{ds_{air}}$ SE X-RAYS

8X TELESCOPIC COLLIMATORS

GRID   GRID

1 2 3 4 5 6 7 8

MIDPLANE

RF HORNS

STRONG LINES EXCITED IN NITROGEN
N_2 SECOND POSITIVE, $N_2(C^3\Pi_u - B^3\Pi_g)$, 337.1 nm
N_2^+ FIRST NEGATIVE, $N_2^+(B^2\Sigma_u^+ - X^2\Sigma_g^+)$, 391.4 nm

SE   SECONDARY ELECTRONS
BSE   BACKSCATTERED ELECTRONS

Figure 2. Test-cell apparatus and diagnostics overview.

laminate absorber on the left side of Fig. 3. Laminate RF absorber applied to the inside curved walls reduced multipath scattering due to reflections from the tank walls.

The lower right hand corner of Fig. 3 shows part of a pressure manifold consisting of four overlapping pressure gauges (1,000 Torr, 100 Torr, 1 Torr, and 50 mTorr) used to monitor the test cell pressure. A small hole in the laminate absorber, not visible in Fig. 3, facilitated rapid equilibration of pressure between the test cell and pressure manifold. Part of an ozone detection system used in prior measurements is visible in the tank but the mirror assembly on the near side of the tank was removed to facilitate installation of the grid system shown in Fig. 3..

Multipath scattering is a primary detractor to a sensitive I/Q system. The grid design in Fig. 3 provides a variable E/N across the midplane and minimizes multipath scattering from the transmission horn to the reception horn. Eight telescopic collimators make chord measurements at 90° to the microwave propagation path. Measurements of the 391.4 nm line from N_2^+ quantified the volumetric ionization rate along the microwave propagation path. Details of the methodology are in Vidmar *et al* [2008 and

4
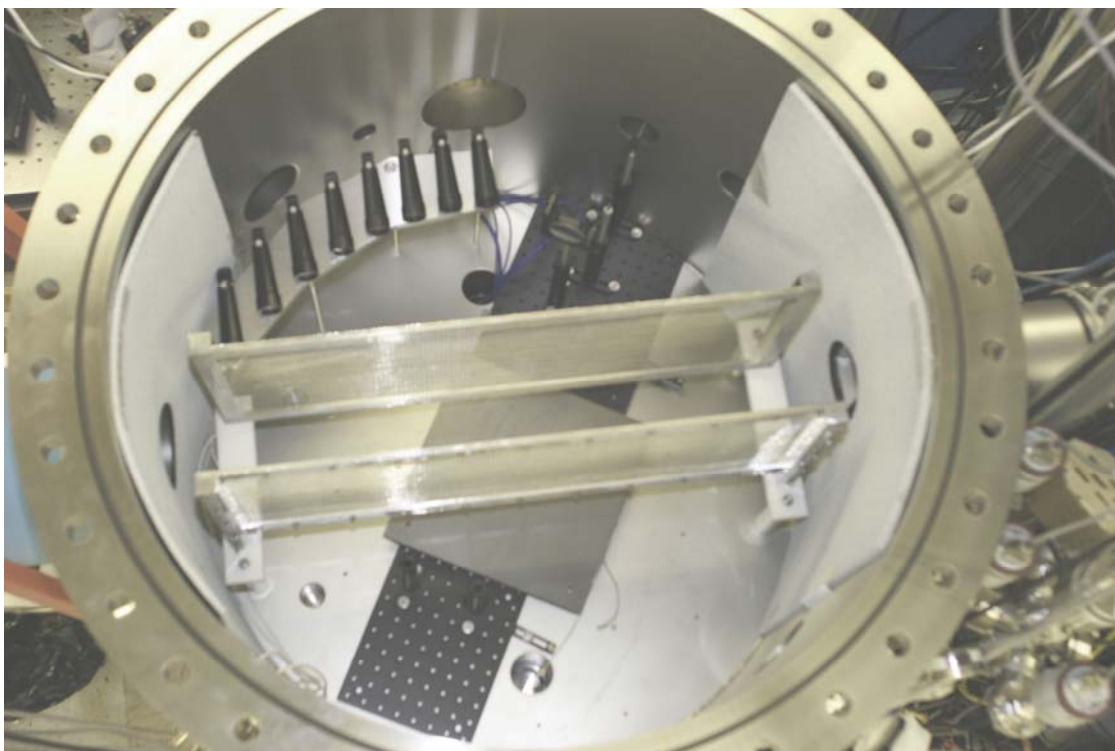
Figure 3. Inside of test cell. RF horns, RF absorber, 8 telescopic collimators, and grid system are all centered on the midplane 12-in from the bottom of the test cell.

2009]. Additional optical observations including ozone, H_2O, N_2O, and CO_2 are in Vidmar *et al* [2008].

The grid system shown in Fig. 3 applies an electric field perpendicular to the RF propagation path and normal to the optical paths of the telescopic collimators. The grids provide low multipath RF propagation from the transmission to reception horn and provide a variable E/N up to 1.2 Td at 60 Torr. A second-generation grid system is under development to increase the E/N value and extend measurements to higher pressure.

B. Microwave I/Q Diagnostics

A microwave diagnostic was used to determine both the electron number density, n_e, and the momentum transfer collision rate, ν, along a chord on the midplane. Heald and Wharton [1965] describe the general technique. The theory for wave propagation in a collisional plasma is based on Maxwell's equations and the Langevin equation that includes a term in the force equation for momentum transfer collisions between electrons and a background gas. The Langevine equation is necessary to model lightly ionized plasmas with air pressure between 1 mTorr and 760 Torr. The dispersion relation relates angular frequency to wave number. Plane-wave propagation is proportional to

$$E(t,z) = E_o exp[+i(\omega t - kz)] \qquad (1)$$

where E is electric field, V/m, t is time, s, z is distance along the propagation path, m, E_o is a reference value for the electric field, V/m, ω (= $2\pi f$) is the angular frequency, s^{-1}, f is frequency, Hz, k = $(2\pi/\lambda)$ is wave number, m^{-1}, and λ is wavelength, m. The wave number for propagation in vacuum, k_o, is given by

$$k_o = \frac{\omega}{c} \qquad (2)$$

The dispersion relation for wave propagation in collisional plasma reduces to an expression for a complex wave number given by

$$k(\omega) = k_r - ik_i = k_o \left[1 - \frac{n_e e^2}{m_e \varepsilon_o \omega(\omega - i\nu)}\right]^{1/2} \qquad (3)$$

where k_r and k_i are the real and complex parts of the wave number, m^{-1}, i = $+(-1)^{1/2}$ is the complex constant, e is the charge on an electron, 1.609×10^{-19} C, me is the mass of an electron, 9.109×10^{-31} kg, and ε_o is the permittivity of free space, 8.854×10^{-12} F/m. The solutions for n_e and ν are extracted from (3) by squaring (3) and separating into real and complex parts

$$k_r^2 - k_i^2 = k_o^2 \left[1 - \frac{n_e e^2}{m_e \varepsilon_o \omega(\omega^2 + \nu^2)}\right] \qquad (4)$$

$$2k_r k_i = -k_o^2 \left(\frac{n_e e^2}{m_e \varepsilon_o}\right)\left(\frac{\nu}{\omega}\right)\left(\frac{1}{\omega^2 + \nu^2}\right) \qquad (5)$$

Equations (4) and (5) are then used to solve for ν and n_e

$$\frac{\nu}{\omega} = -\frac{2 k_r k_i}{k_o^2 - k_r^2 + k_i^2} \qquad (6)$$

6

$$n_e = \frac{m_e \varepsilon_o c^2}{e^2}(k_o^2 - k_r^2 + k_i^2)\left[1 + \frac{4\,k_r^2\,k_i^2}{(k_o^2 - k_r^2 + k_i^2)^2}\right] \qquad (7)$$

Equations (6) and (7) permit solution of n_e and ν in terms of the microwave frequency, the complex wave number, and physical constants. The method has been in use for over 45 years and produces excellent results.

A system to measure the complex wave number is significantly simpler today than when it was first introduced. Excellent results are possible in a system that only depends on a few high-quality modern components. The In-phase and Quadrature (I/Q) detection system in Fig. 4 was build and used to measure the magnitude and phase of the RF signal propagating through the test cell with and without plasma present. The critical components are a stable signal generator, a high-quality low-noise linear amplifier, and a high-quality I/Q detector selected for amplitude and phase response linearity. A stable 10 GHz RF signal from the generator connects to a 6-dB coupler with the main signal coupled to the transmit horn in the test cell. The 6-dB coupler also couples to the LO port of the I/Q detector through an isolator, not shown in Fig. 4. The main signal propagates across the test cell and couples to the receive horn

Figure 4. I/Q detection system overview.

with a net signal loss of 15.2 dB. Plasma along the propagation path exists near the center of the propagation path and roughly extends ± 15 cm from the centerline of the test cell. A 32-dB 10-GHz low-noise amplifier, LNA, amplifies this signal. A power divider splits the power equally and couples to a power measuring system and to the RF port of the I/Q detector. A spectrum analyzer or a diode detector monitors the power level coupled into the RF port. Additional attenuators are installed in the system to lower the signal level at the RF port of the I/Q detector to a value that optimizes linearity. There are also several isolators installed to reduce unwanted reflections.

As shown in Fig. 4, the I/Q detector consists of two mixers: one driven in-phase by the LO, the In-phase or I channel, and one driven with a 90° phase shift, the quadrature or Q channel. The quality of the I/Q detector governs the overall sensitivity of the detection system. Aspects of quality is the accuracy of the power split of the RF signal to the mixers, the accuracy of the power split and phase shift network of the LO signals, and the balance of the diodes for both mixers. Additional details of this system down to the part numbers are in the Appendix.

The outputs of the I/Q detector define a phasor with respect to the LO reference signal. That phasor in terms of Cartesian and polar coordinates is

$$V_{I/Q} = V_I + iV_Q = |V_{I/Q}|exp(+i\Delta\phi) \tag{8}$$

When plasma is present, the transient plasma signal is measured using AC coupling between the I/Q outputs to low-noise amplifiers, which are subsequently filtered to improve their signal-to-noise ratio (SNR). These transient signals represent the change in the phasor due to plasma. The phasor perturbations on the I and Q channels are designated ΔV_I and ΔV_Q and are recorded on a digital sampling oscilloscope (DSO). The resulting DSO signals relate to ΔV_I and ΔV_Q via

$$V_{I, DSO} = G_I\Delta V_I \tag{9}$$

$$V_{Q, DSO} = G_Q\Delta V_Q \tag{10}$$

where G_I and G_Q are the gains of the LNAs for the I-channel and Q-channel, respectively.

The acquisition of data begins with a measurement of the phasor associated with free space conditions or those present in the test cell prior to plasma generation. The free space or reference measurements of the I and Q channels are denoted by $V_{I,R}$ and $V_{Q,R}$ and shown in Fig. 4 as measurements made with good quality battery powered voltmeters. These measurements define a free-space reference vector

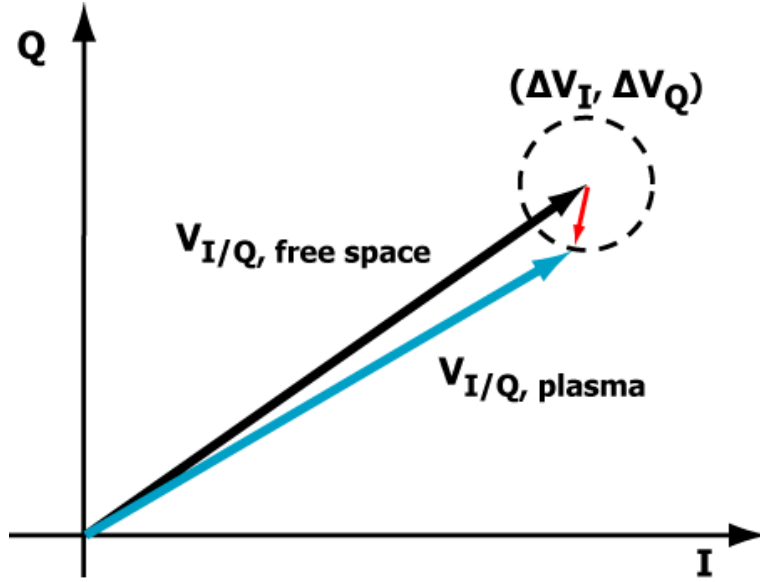$$V_{I/Q, free space} = V_{I,R} + i V_{Q,R} \tag{11}$$

Figure 5. Vector addition to form plasma phasor from of free-space and plasma perturbation phasors.

When plasma is present, the plasma phasor is the vector sum of the free space and transient phasors shown in Fig. 5. Algebraically, the plasma phasor is

$$V_{\text{I/Q, plasma}} = V_{\text{I/Q, free space}} + \Delta V_I + i\,\Delta V_Q \qquad (12)$$

The phasors defined in Eqs. 11 and 12 quantify wave propagation through the test cell. The phase and amplitude changes represented by the microwave measurements require interpretation in terms of the plasma present in the test cell.

The phasor measurements in conjunction with two assumptions lead to the determination of the complex wave number. The first assumption is that plane wave propagation, Eq. 1, is an adequate model in the plasma. The second assumption is that the complex wave number is constant over a distance ℓ through the plasma. Under these assumptions, the phase change and amplitude change of the phasors permit solution for the complex wave number of a uniform collisional plasma slab. The equation for the change in phase from free space to plasma conditions provides an equation to evaluate k_r.

$$\Delta\phi = \phi_{free\,space} - \phi_{plasma} = -(k_o - k_r)\ell \qquad (13)$$

The ratio of the plasma and free space phasors provides an equation to evaluate k_i.

$$A(dB) = 20\,log_{10}\left[\frac{\left|V_{I/Q,\,plasma}\right|}{\left|V_{I/Q,\,free\,space}\right|}\right] = +8.686\,k_i\,\ell \qquad (14)$$
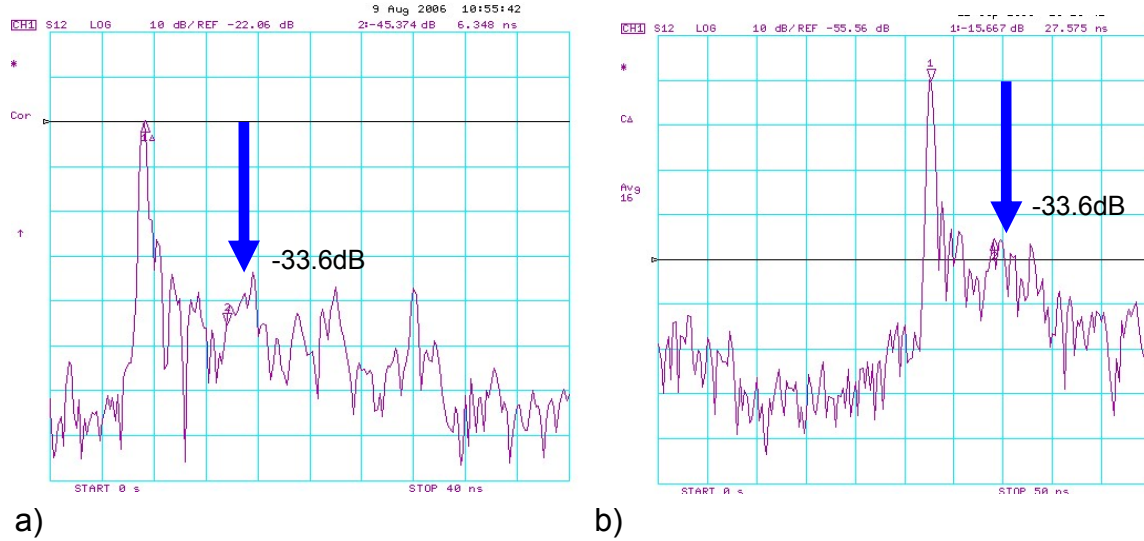
9

Figure 6. Time domain S_{12} of internal reflections between transmission and reception horns at 10 GHz with absorber. a) System prior to insertion of grids.. b) System with grids present.

The experimental values of the complex wave number used in Eqs. 6 and 7 yield experimental values for ν and n_e.

One complication with such phase and amplitude measurements is multipath scattering between the transmission and reception horns. Unwanted reflections would add into the received signal, confuse the phase measurement, and limit overall sensitivity. The design of the grid system shown in Fig. 3 minimized reflections by bringing the grids close to the tank walls and extending well above and below the centerline for RF propagation. Measurements of multipath, before and after adding the grid system to the test cell, quantified multipath scattering. The spectrum analyzer plots in Fig. 6 are in the time domain and quantify the main signal and subsequent reflections. Before the addition of the grid assembly, the multipath contribution to the main signal is 33.6 dB below the main signal, as shown in Fig. 6a. After installing the grid assembly, another measurement produced the same result, a shown in Fig. 6b. Consequently, the current grid does not introduce unwanted multipath. A second-generation grid could be set back from the tank walls and the height decreased, which would permit grid operation at higher E/N values.

An example of raw data from the DSO that quantifies the plasma phasor perturbation appears in Fig. 7. The I and Q channel signals change from their quiescent values when the electron beam is present. The free-space phasor preceding this shot was $V_{I,R}$ = + 20.33 mV and $V_{Q,R}$ = 44.42 mV, which puts it in the first quadrant as shown in Fig. 5. For an ideal I/Q detector the phasor would have constant magnitude and sweep out a perfect circle as the phase varied. Prior to measurements with the I/Q detector, the frequency was slowly varied and the maximum and minimum values of I and Q were recorded. These measurements quantified the I and Q voltage
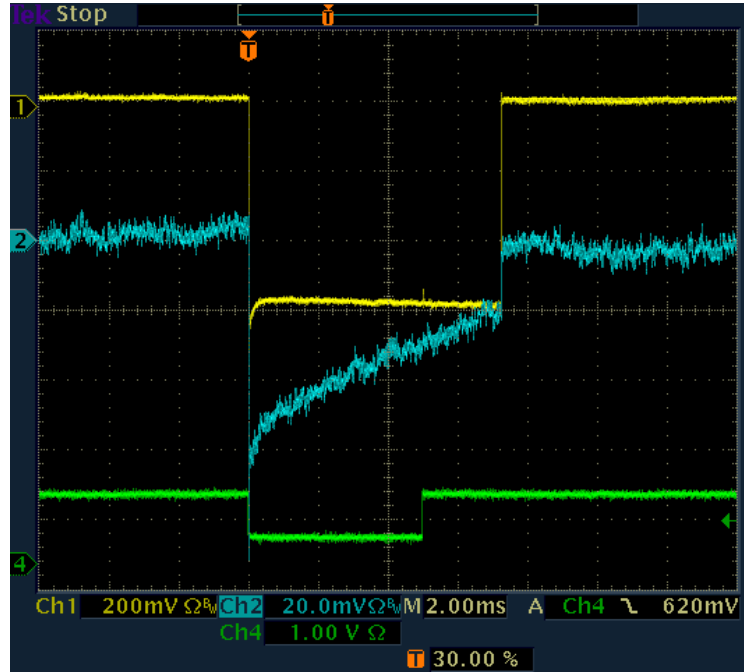
Figure 7. Shot 009 on 14 Oct 2009: 60 Torr test-cell pressure, 1,660 V grid potential difference, 7-ms duration pulse, 100 kV electron beam energy, and 2.56 mA beam current incident on transmission window. Channel 1 is the I signal, channel 2 is the Q signal, and channel 4 is a 5-ms trigger pulse for the electron beam. All measurements made with $G_I = G_Q = 2{,}000$, 100- kHz LPF, and 50-kHz LPF post filtering. This data corresponds to initial values of $n_e = 6.73 \times 10^8$ cm^{-3} and $\nu = 3.57 \times 10^{10}$ s^{-1} and final values of $n_e = 6.47 \times 10^8$ cm^{-3} and $\nu = 3.03 \times 10^{10}$ s^{-1}.

offsets, 3.31 mV and 7.40 mV, respectively. These measurements also quantified the span of the I and Q voltages, 117.54 mV and 112.8 mV. The calculation of the free-space phasor includes corrections for these offsets and span differences.

In Fig. 7, the sensitivity of the I channel is 200 mV/division. The net gain for the I and Q channel amplifiers is 1,000, when used with 50-Ω termination. The I-channel transient is -61.2 μV, and the Q-channel transient is -62.2 μV at the leading edge of the plasma pulse. A 5-ms trigger pulse to the electron source produced a 7-ms pulse. At the end of the pulse, the Q-channel transient is -24.0 μV. These values were used to construct a plasma phasor and to evaluate n_e and ν as noted in the caption for Fig. 7.

The current sensitivity of the I/Q detector is 0.0075 rad (0.43 deg) and 0.032 dB. Noise associated with the output amplifier of the SR 560 in Fig. 4 is limiting sensitivity. The issue is broadband noise generation for amplifier gains in excess of 1,000. The 50-kHz 40-dB LPF following the SR 560 addresses that issue and significantly reduces high frequency noise. A filter with a sharper cutoff and greater attenuation could improve the current SNR by an additional factor of 5 to 10.

C. <u>Optical Determination of Electron Density Profile</u>

As noted in the above section, the complex wavenumber depends on the length of plasma along the RF propagation path. Optical measurements reported in Vidmar *et al* [2009] quantify N_2^+(0-0) First Negative emissions at 391.4 nm. The emissions detected at 10 Torr use the 1st, 3rd, 5th, and 7th collimators in Fig. 3. The optical path of the first collimator is perpendicular to the RF propagation path and crosses the center of the test cell.

The first negative emission from N_2^+ is a byproduct of high-energy electron impact ionization of air. A fraction of the nitrogen ionized by the electron beam is in an excited state that results in an emission at 391.4 nm. The yield of emissions per high-energy electron is constant, so the light intensity at 391.4 nm is proportional to the number of excitation events. This emission is proportional to the volumetric ionization rate of the electron beam. An air-chemistry code establishes the relation between the volumetric ionization rate and the electron density. A 100 keV electron beam with a beam current of 2-3 mA produces a volumetric ionization rate from 1×10^{14} 1/cm^3-s to 5×10^{14} 1/cm^3-s in 60 Torr air. Figure 8 shows the electron density as a function of E/N for constant values of ionization rate. The curve for $R = 3 \times 10^{14}$ 1/cm^3-s is close to the experimental valued deduced from ozone measurements. The curves show a nearly linear relationship between electron density and E/N. This relationship deviates slightly for E/N greater than 1.5×10^{-18} V-cm^2. A linear relationship between N_2^+ optical emissions and electron density permits estimation of the electron density profile.
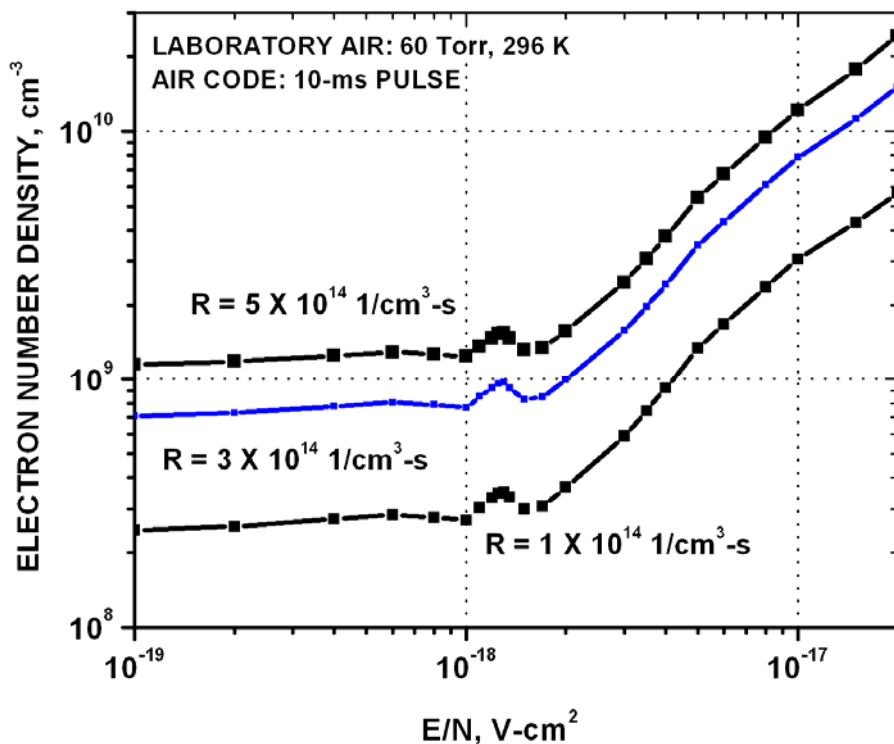

Figure 8. Electron density as a function of E/N for constant volumetric ionization.

The eight telescopic collimators in Fig. 3 collect light along chords perpendicular to the RF propagation path. With the grids present, the free-space transmission factor for the grids reduces the light collected from each of the 8 channels by 24%. The first channel in Fig. 3 is the telescopic collimator directly in front of a 8-in port and has the longest chord of all the telescopic collimators. The channels numbers are from 1 to 8 with 1 the longest chord and 8 the smallest. Because the transmission factor is the same for all of the telescopic collimators, the effect of the grids is to reduce the count rate in each telescopic collimator, so the relative count rate between channels is not affected. An example of the N_2^+ optical emissions centered on 391.4 nm is in Fig. 9. The intensity is highest at the center of the test cell with y = 0. The intensity decreases for the 3rd collimator at y = 10 cm, and decreases substantially for the 5th and 7th collimators at y = 20 cm and y = 30 cm.

Measurements of count rate as a function of pressure provided data by which to estimate the electron density profile. The analysis by Vidmar *et al* [2009] quantifies the data and methodology for determining the volumetric ionization profile. At pressures below 100 mTorr, the optical count rates decreased to the noise level and so provided no information on the volumetric ionization profile. For pressures below 100 mTorr, MAGIC code calculations provided an estimate of the spatial electron beam profile. Because the volumetric ionization rate is proportional to the electron beam current density, the MAGIC calculations extended the volumetric ionization profile to low pressures.
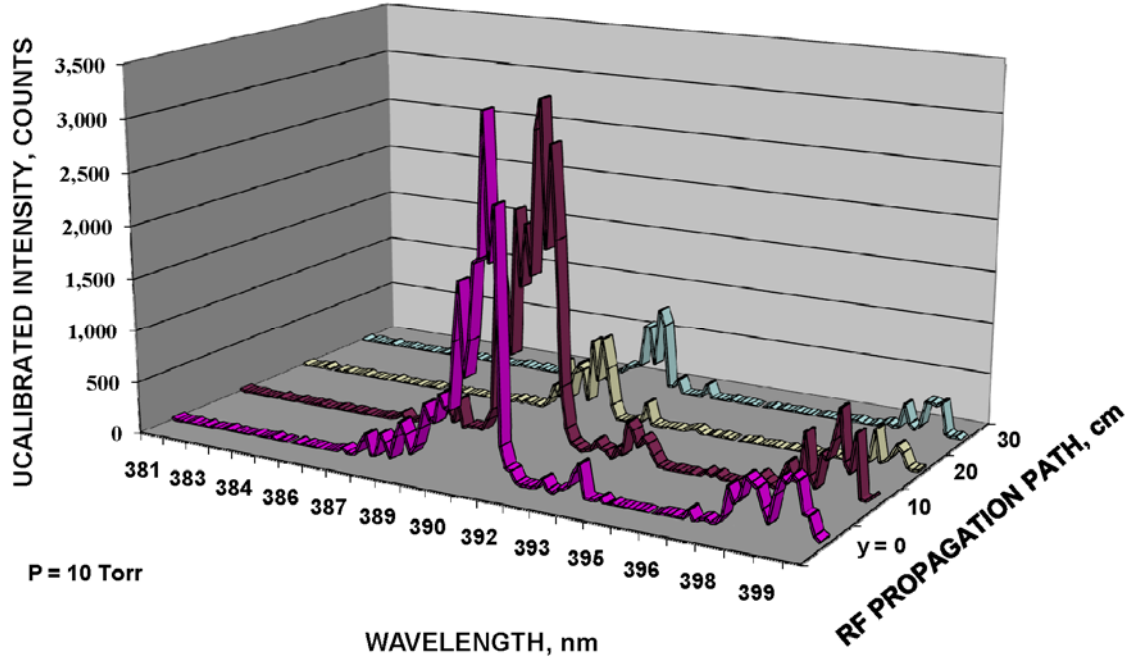

Figure 9. Nitrogen optical emissions from plasma detected by the 1st, 3rd, 5th, and 7th collimators aligned perpendicular to the RF propagation path.
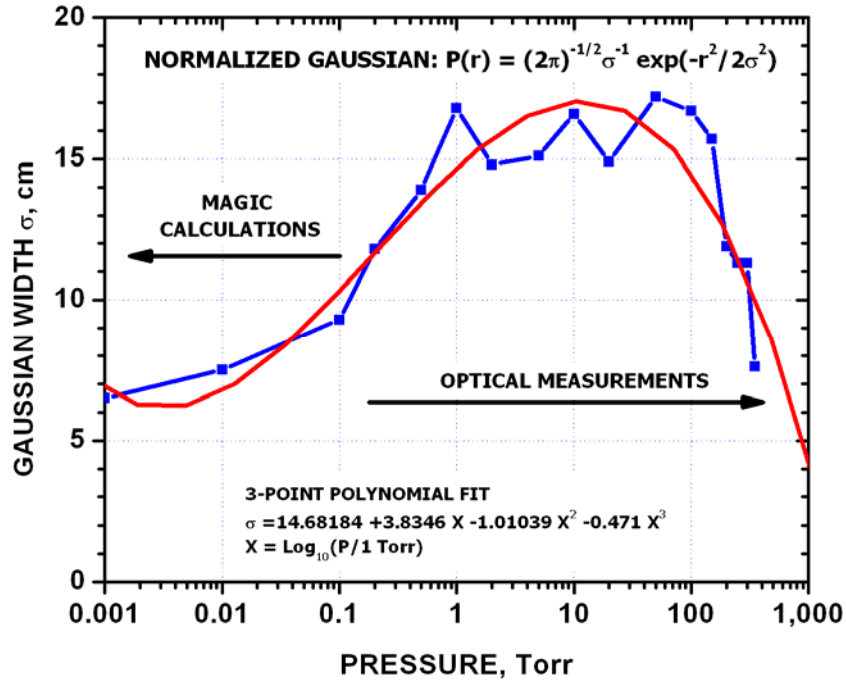
Figure 10. Electron-beam Gaussian profile at midplane.

As noted above and in Fig. 8, the electron density is nearly proportional to the volumetric ionization rate. The optical intensity data at each pressure point in Fig. 10 provided the Gaussian width for a normalized Gaussian profile. The Gaussian half widths as well as a 3-point polynomial fit to the data appear in Fig. 10. The initial beam diameter is 6 cm at the transmission window foil. At pressures below 1 Torr, the Gaussian half width is relatively constant and derives its width from the additional beam divergence due to scattering through the transmission window foil. At pressures from 1 Torr to 100 Torr the Gaussian half width increases to a maximum due to electron beam divergence as it transits the gas from the transmission window to the midplane, approximately 25 cm (10-in). At pressures above 100 Torr, the electron-beam range decreases and pulls away from the midplane decreasing the Gaussian half width. Optical emissions were essentially unaltered by the application of E/N ranging from 0.01 Td to 1 Td.

D. Reduced Electric Field Measurements

The grids in Fig. 3 are made of 304 stainless steel wire mesh with 32-mil diameter wires, 76% open area, and is of welded construction. The mesh covers an aluminum frame that is 31-in long and 12-in high. There is a 6-in separation between grids and the grids are electrically isolated from the inside of the test cell. One grid is biased positive and the other is biased negative. High-voltage power supplies feed 5-μF capacitor banks, which feed the grids through 10-Ω power resistors. A high voltage sensing system monitors the voltages across the power resistors. A DSO records the current flow through these resistors, when plasma is present. The design of the grid system was to apply an E/N of up to a few Td and not to interfere with the microwave measurements. As shown in Fig. 6, the grids do not interfere with the RF measurements. Electrical measurements of the grid current were not useful in estimating plasma conductivity as the measurements indicated current flow to the inside walls of the test cell. A second-generation grid design will provide additional separation between the grids and the test-cell walls.

The voltage applied to the grids produced an E/N between the grids. When plasma was present, current flowed from the capacitor banks through the plasma and a RF measurement of the momentum-transfer collision rate quantified the value of E/N. A table of ν as a function of E/N and interpolation provided the value of E/N used for experimental results. A better way to quantify E/N is from the applied voltage. That method needs to wait for installation of a second-generation grid system as noted above.

An air-chemistry code described in Vidmar *et al* (2003, 2004, and 2005) provided a method of modeling electron beam ionization and deionization of air. Theoretical curves in Fig. 11 quantify the overall magnitude of power reduction to generate and sustain plasma as a function of E/N for electron number densities of 10^8 cm^{-3}, 10^9 cm^{-3} ,and 10^{10} cm^{-3} and a pressure of 60 Torr. For the curves in Fig. 11a, the electron number density is constant and the volumetric ionization rate and Joule heating vary to provide sufficient ionization to establish the target electron-number density. The power densities plotted in Fig. 11a consists of two parts shown in Fig. 11b: volumetric ionization from the electron beam and Joule heating, J•E, produced by an applied electric field. For low E/N, power from the electron beam dominates. For high E/N Joule heating dominates.

As E/N increases, the reaction rate for two-body collisional electron detachment from O_2^- increases

$$O_2^- + N_2 = e + O_2 + N_2 \tag{15}$$

The power density decreases slightly from 0.01 TD to 0.06 TD. Power increases to a local maximum near 0.1 Td, as the reaction rate for three-body electron attachment to oxygen increases
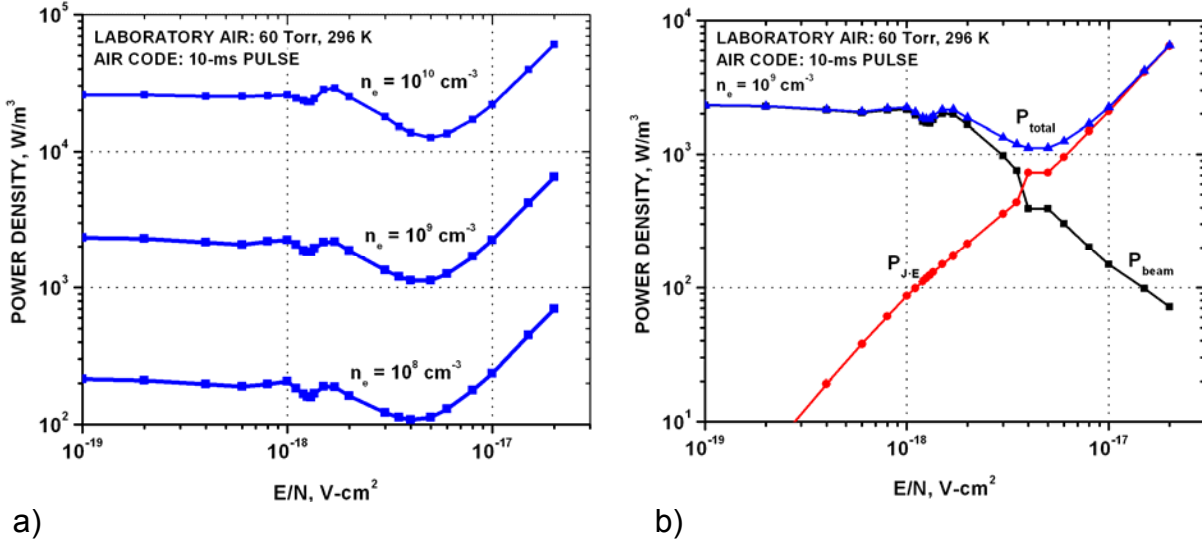
Figure 11. Theoretical curves of power required to generate and sustain plasma as a function of E/N at 60 Torr. a) Total power vs E/N. b) Total power, beam power, and J•E vs E/N.

$$e + O_2 + O_2 = O_2^- + O_2 \tag{16}$$

Power decreases then rises again as the two reactions above compete to detach or attach electron. The nearly equal processes occur between 0.10 Td and 0.17 Td. Above 0.17 Td, some electrons have sufficient energy and collisional detachment of an electron from O^- becomes a competing process

$$e + O^- = e + e + O \tag{17}$$

Power decreases for E/N in the range from 0.17 Td to .40 Td as rate of detachment exceed the attachment processes. Above 0.40 Td, additional recombination and attachment processes dominate over the detachment processes, and the power density increases.

The curves in Fig. 11 suggest that power reduction by a factor of 2 (3 dB) is possible at an E/N value of approximately 0.40 Td (4×10^{-18} V-cm^2). The energy to ionize O_2^- is 0.429 eV. At 0.4 Td, electrons detach from O_2^- consuming less energy than that necessary to generate a free electron via high-energy impact ionization (33.7 eV).

The experimental curves in Fig. 12 represent the electron number density and momentum transfer collision rate as a function of E/N. As noted earlier, the experimental value of the momentum-transfer collision rate provided the value of E/N via a table of momentum-transfer collision rate versus E/N. An additional issue with that approach is the gas composition at 60 Torr. Because the RF laminate absorber has a large surface area and the test cell has a surface area of 3 m^2, outgassing of water vapor may be an issue at low pressure. The water vapor concentration in the test cell
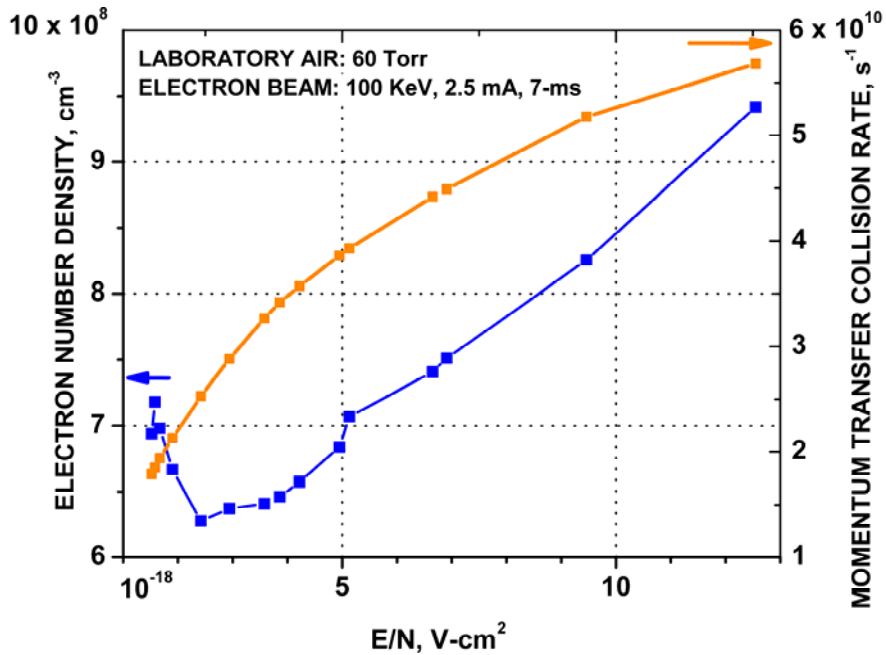
Figure 12. Experimental values of electron number density and momentum-transfer collision rate versus E/N.

may be higher than the 75% relative humidity used in calculations. Any error in water vapor concentration would change the E/N value attributed to a particular value of momentum-transfer collision rate. The E/N scale may need expansion or compression depending on the exact water vapor concentration.

During the experiment, there was a shot-to-shot variation in electron beam current. For the data in Fig. 12, taken in Oct 2009, the beam current ranged from 2.32 mA to 3.02 mA. Hence, there is a 30% variation in the volumetric ionization rate. Because the electron number density and volumetric ionization rate exhibit a rough linearity over small changes in the volumetric ionization rate, the electron number density was normalized to the volumetric ionization rate for a 2.5 mA beam current. There is a dip in electron number density from approximately 0.10 Td to 0.5 Td that can be attributed to electron three-body attachment to oxygen. The increase in electron density predicted in Fig. 11 does not appear in the experimental data. As noted previously, the grid system was shorting to the return ground when plasma was present.

An alternative method to generate an electric field in plasma is to rely on the axial electric field in a pulsed electron beam. This does not rely on any external grids or power supplies and is a practical means for volumetric ionization with an imposed electric field. Because the 1/e plasma lifetime in a 60 Torr air plasma is approximately 1.5 μs, an on-off pulse sequence with 1 μs between pulses would maintain an electron concentration of approximately 50% of the maximum electron density generated during a pulse. MAGIC code simulations provide estimates of axial electric field and E/N during a short pulse as a function of electron-beam current for a geometry identical to

Table 1 Axial Electric Field vs Electron Beam Current

Beam Current A	Axial Electric Field V/m	E/N V-cm^2
0.010	-0.976	3.0×10^{-21}
0.100	-7.83	3.0×10^{-20}
1.0	-107.4	3.5×10^{-19}
10.0	-816.3	3.5×10^{-18}
20.0	-1,446	6.5×10^{-18}

Data: Air-plasma test cell geometry, air at 60 Torr, 100 keV electron energy, axial field 25 cm from source.

the air-plasma test cell. The results in Table 1 indicate a beam current between 10 A and 20 A is necessary to produce an E/N of approximately 4×10^{-18} V-cm^2. The electron beam normally operates at 2 mA to 3 mA and a fresh firing unit in the electron source brings the current up to 20 mA. Kimball Physics indicates their source could operate at the 1 A level for short pulses, but the system would need additional energy storage capacitors. Operation at the 10 A to 20 A level requires a reworking of the source. It would be simpler to start with a new source rated for 20-A pulses to produce axial fields of 0.4 Td.

Resolution of the above issues requires a new grid system and more energy storage for the grid system and/or a new electron beam source. A second-generation grid and energy storage system is the most inexpensive option.

E. <u>Automation of Data Acquisition</u>

When conducting an experiment, data is generated on two 4-channel DSO and a spectrometer. Data collection was by hand and recorded in a logbook. The process took a long time and limited the number of shots per day. It became clear that some form of automation was necessary as data collection was becoming a limiting process. To that end, LabView was used to automate as much of the data acquisition as was feasible. A LabView program now captures screen shots of the DSOs and stores them in a data file. Because of systematic changes in received power due to changes in test-cell pressure and temperature changes that affected the transmission of signal in RF cables, the I/Q calibration varies during the day. A LabView program automates the calibration of the I/Q detector. That system varies the source frequency in small steps to simulate a 360° phase change and determines the maximum and minimum voltages of the I and Q. That data provides the DC offset voltages and span for the I and Q channels, which are necessary to evaluate phasors accurately.

III RESULTS

The results of this project are the following.

- Theoretical predictions of a factor of two reduction in power for electron-beam generation and sustainment with an E/N of approximately 0.4 Td.

- First round of experiments as a function of E/N that varies from 0.1 to 1 Td conducted at 60 Torr for electron-beam generated plasma.

- First-generation grid, capacitor bank, high-voltage charging system, and a discharge current sensing system fabricated, installed, and used.

- Optical measurements of electron density profile along the RF propagation path conducted as a function of pressure and in the presence of an applied electric field.

- Refinements to an in-phase and quadrature detector system increased sensitivity.

- MAGIC code calculations quantify electron source parameters to generate axial electric field.

IV PERSONNEL, INTERACTIONS, AND PUBLICATIONS
1 Dec 2006 – 30 Nov 2009

Personnel. The primary personnel on this project has been

- Robert J Vidmar, Principal Investigator

- Kenneth R Stalder, Consultant

Interactions. Presentations and publications based on this project were presented at the 60th, 61st, and 62nd Gaseous Electronic Conferences, and at the 46th and 47th Aerospace Sciences Meeting and Exhibit American Institute of Aeronautics and Astronautics Conference, 35th and 36th International Conference on Plasma Science. There were many interactions with representatives from DoD Laboratories, National Laboratories, private companies, and Universities from around the world.

Publications Supported by AFOSR Grant Number FA9550-7-0021

Vidmar, R., and K. Stalder, "Electrical and Optical Diagnostics of an Electron-Beam Generated Air Plasma," Oral Presentation PR1-53, 60th Annual Gaseous Electronics Conference, 2-5 Oct 2007, Arlington, VA, GEC07, 2007, Bulletin of the American Physical Society, Vol 52, No 8, p 48,ISSN 0003-0503(200710)52:8;1-L, 2007.

Vidmar, R., and K. Stalder, "Electron-Beam Generated Air Plasma: Electrical and Optical Diagnostic Details," Poster Presentation SRP1 16, 60th Annual Gaseous Electronics Conference, 2-5 Oct 2007, Arlington, VA, GEC07, 2007, Bulletin of the American Physical Society, Vol 52, No 8, p 58, ISSN 0003-0503(200710)52:8;1-L, 2007.

Vidmar, R., M. Seeley, A. Y. Serdyuchenko, and K. Stalder, "Electrical, RF, and Optical Diagnostics in E-Beam Excited Air Plasma," Session 191-PDL-7, AIAA 2008-1111, p 17, 46th Aerospace Sciences Meeting and Exhibit, Reno, NV, 7-10 Jan, 2008.

Vidmar, R.J., and K. R. Stalder, "Electron-Beam Generated Air Plasma: Measurement of Ozone and Electron Density," 35th IEEE International Conference on Plasma Science, 15-19 June 2008, Karlsruhe, Germany, Poster 1P25, June 2008.

Vidmar, R.J., and K. R. Stalder, "Electron-Beam Generated Air Plasma: Ozone and Electron Density Measurements," 35th IEEE International Conference on Plasma Science, 15-19 June 2008, Karlsruhe, Germany, Oral 4A8, June 2008.

Vidmar, R.J., C. Ramsayer, and K.R. Stalder, "Microwave In-Phase and Quadrature Detection of E-Beam Generated Air Plasma," Poster Presentation LW1 4, 61st Annual Gaseous Electronics Conference, 13-17 Oct 2008, Dallas, Texas, Bulletin of the American Physical Society, Series II Vol 53, No 10, p 48, ISSN 0003-0503, Oct 2008.

Vidmar, R.J., C. Ramsayer, and K.R. Stalder, "Electron-Beam Generated Air Plasma: Microwave I/Q Detection of Plasma Properties and Optical Measurements of Nitrogen and Ozone to Quantify Plasma Spatial Distribution," Oral Presentation MWP1 16, 61st Annual Gaseous Electronics Conference, 13-17 Oct 2008, Dallas, Texas, Bulletin of the American Physical Society, Series II Vol 53, No 10, p 53, ISSN 0003-0503, Oct 2008.

Vidmar, R., D. Kumari, C. Ramsayer, and K. Stalder, "Electron-Beam-Generated Air Plasma: Microwave Diagnostics and Optical Measurements," Session 188-WIG-9/PDL-19, AIAA-2009-1049, p 12, 47th Aerospace Sciences Meeting and Exhibit, Orlando, FL, 5-8 Jan, 2009.

Vidmar, R.J., A. Uppaluri, C. J. Ramsayer, and K. R. Stalder, "Electron-Beam Produced Air Plasma: Electron Density and Momentum-Transfer Collision Rate Measurements," 36th IEEE International Conference on Plasma Science, 21 May – 5 June, San Diego, CA, Oral presentation IO2A-8, June 2009.

Vidmar, R.J., A. Uppaluri, C. J. Ramsayer, and K. R. Stalder, "Electron-Beam Produced Air Plasma: I/Q Detector and Optical System Used to Measure Electron Density and Momentum-Transfer Collision Rate," 36th IEEE International Conference on Plasma Science, 21 May – 5 June, San Diego, CA, Poster IP3G-43, June 2009.

Vidmar, R.J., and A. Uppaluri, "X-Ray Induced Breakdown in Air with High Reduced Electric Field" Oral Presentation PW3.00004, 62nd Annual Gaseous Electronics Conference, 20-23 Oct 2009, Saratoga Springs, New York, Bulletin of the American Physical Society, Series II Vol 54, No 12, p 61, ISSN 0003-0503, Oct 2009.

Vidmar, R.J., and A. Uppaluri, "X-Ray Induced Breakdown in Air at High Reduced Electric Field: Experimental Details" Poster Presentation URP.00071, 62nd Annual Gaseous Electronics Conference, 20-23 Oct 2009, Saratoga Springs, New York, Bulletin of the American Physical Society, Series II Vol 54, No 12, p 87, ISSN 0003-0503, Oct 2009.

Vidmar, R.J., A. Uppaluri, and K. Stalder, "Electron-Beam Generated Air Plasma Measurements: Effect of Reduced Electric Field" Oral Presentation JT2.00002, 62nd Annual Gaseous Electronics Conference, 20-23 Oct 2009, Saratoga Springs, New York, Bulletin of the American Physical Society, Series II Vol 54, No 12, p 32, ISSN 0003-0503, Oct 2009.

Vidmar, R.J., A. Uppaluri, and K. Stalder, "Electron-Beam Generated Air Plasma Measurement Details: I/Q Detector and Effect of Reduced Electric Field" Poster Presentation URP.00082, 62nd Annual Gaseous Electronics Conference, 20-23 Oct 2009, Saratoga Springs, New York, Bulletin of the American Physical Society, Series II Vol 54, No 12, p 89, ISSN 0003-0503, Oct 2009.

REFERENCES

Heald, M. A., and C. B. Wharton, *Plasma Diagnostics with Microwaves*, John Wiley & Sons, New York, NY, PP 117-154 and 192-220, 1965.

Vidmar, R. J., and K. R. Stalder, "Air Chemistry and Power to Generate and Sustain Plasma: Plasma Lifetime Calculations," AIAA 2003-1189, p 8, Jan, 2003.

Vidmar, R. J., and K. R. Stalder, "Electron-Beam Generated Plasma in Air: Pulsed and Continuous Generation," AIAA 2004-359, p 8, Jan, 2004.

Vidmar, R. J., and K. R. Stalder, "Air-Plasma Experimentation at the University of Nevada, Reno," AIAA 2005-0791, p 12, Jan, 2005.

Vidmar, R., M. Seeley, A. Y. Serdyuchenko, and K. Stalder, "Electrical, RF, and Optical Diagnostics in E-Beam Excited Air Plasma," Session 191-PDL-7, AIAA 2008-1111, p 17, 46th Aerospace SciencesMeeting and Exhibit, Reno, NV, 7-10 Jan, 2008.

Vidmar, R., D. Kumari, C. Ramsayer, and K. Stalder, "Electron-Beam-Generated Air Plasma: Microwave Diagnostics and Optical Measurements," Session 188-WIG-9/PDL-19, AIAA-2009-1049, p 12, 47th Aerospace Sciences Meeting and Exhibit, Orlando, FL, 5-8 Jan, 2009.

APPENDIX

I/Q DETECTOR DETAILS   A-2

FIGURES

I/Q DETECTOR DETAILS

The I/Q detector evolved over several years into the device shown in Fig. A1. All components were mounted in a copper box with 5/8-in wide side walls and 1/4-inch base and top plates. A 5/8-in panel separates the transmission and reception sides and isolates the high power region for the transmission horn from the I/Q detector reception side. The copper box provided a massive heat sink for the low-noise RF amplifier. Screws fastened components to the base plate or sidewalls. Grounding and touch sensitivity issues greatly diminished. The schematic in Fig. A2 provides part numbers and power levels used during normal operation. The attenuator, phase shifter, and transfer switch connected by green lines in Fig. A2 permit small changes in power levels to the RF transmission horn. This subsystem is useful in characterizing the I/Q detector sensitivity. Several additional isolators in Fig. A2 eliminated reflections, and increased overall sensitivity. A 4-ft RF cable connects the output of the receive horn to the RF IN port in Fig. A1. A 16-ft low loss cable connects the RF OUT port to the transmit horn.

The Miteq Inc. I/Q detector used in Fig. A1 has part number IQM0812LC2Q and a 8-12 GHz bandwidth. The I/Q detector has two mixers: one driven at 0° with respect to the LO and the other at 90°. A splitter divides power from the RF port into two equal parts, which then drives the two mixers. The output from the mixer driven by the LO
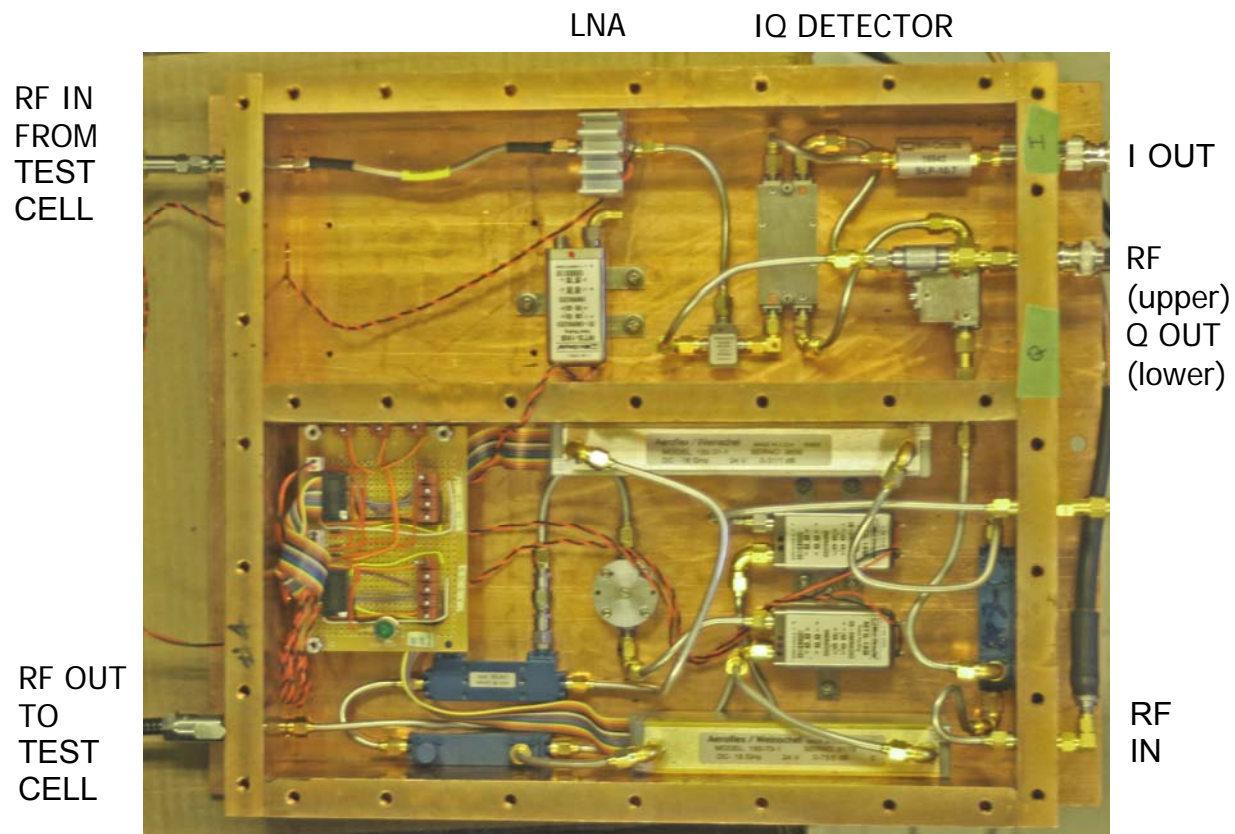

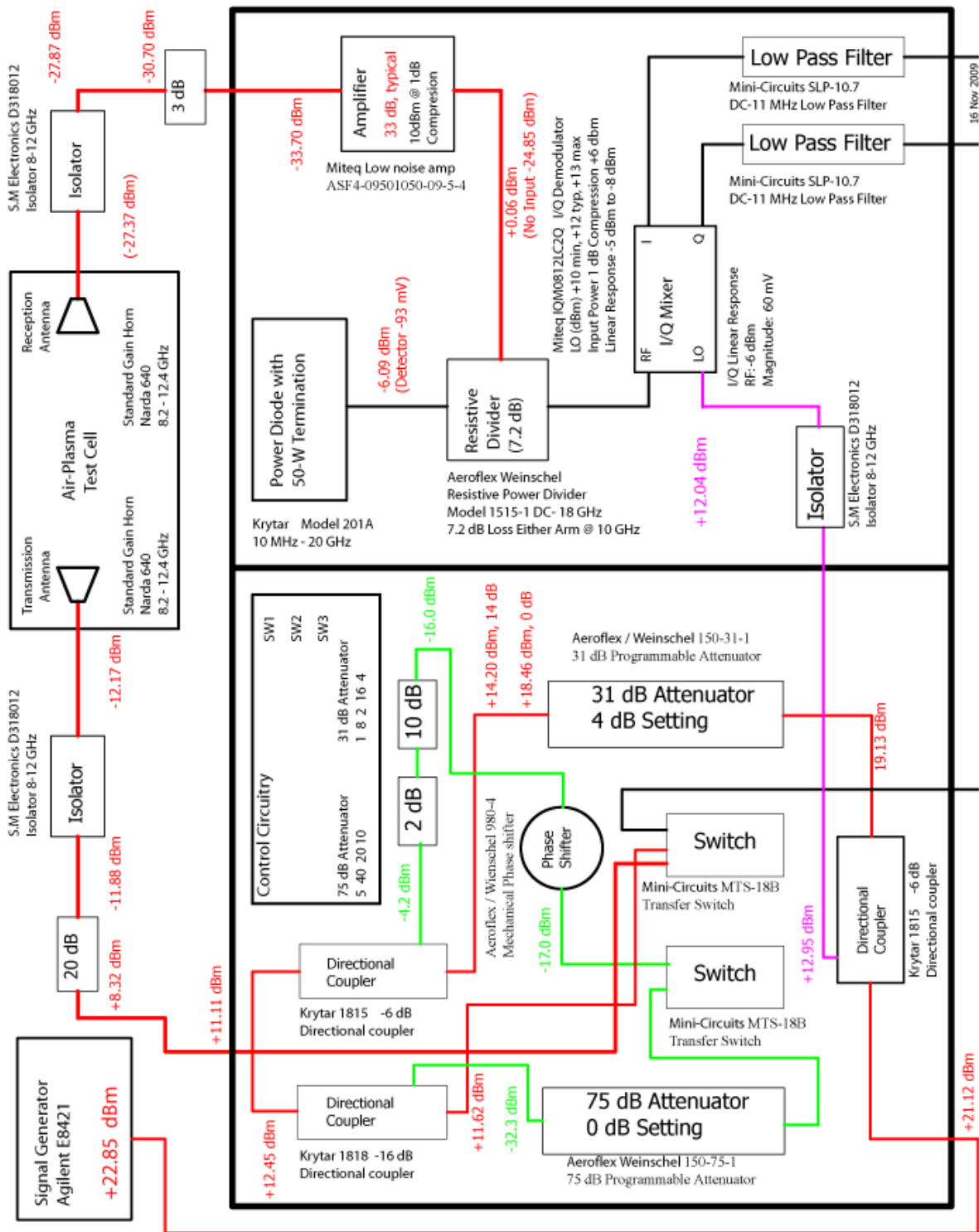Figure A1. I/Q detector hardware on 9 Nov 2009.

Figure A2. I/Q detector schematic and power levels.

with 0° phase shift is the In-Phase or I channel. The mixer driven by the LO with a 90° phase shift is the Quadrature or Q channel. These two outputs provide a decomposition of the RF signal into in-phase and quadrature components. The I and Q outputs define a phasor of the RF signal with respect to the LO.

The linearity of the I /Q detector was investigated as a function of power to its RF port. Fixed attenuators applied to the input of the LNA systematically decreased the power to the I/Q RF port in 1 dB steps. Figure A3 quantifies the results of the I/Q detector output and defines the region of maximum linearity. A 3 dB attenuator inserted to the RF IN from the test cell resulted in -6 dBm applied to the RF port and produced maximum I/Q linearity. As the RF power level decreased to -6 dBm the overall phasor magnitude decreased to approximately 50 mV. The I and Q DC offsets were 3.3 mV and 7.4 mV, respectively. Factoring these offsets into the phasor magnitude improves magnitude accuracy.
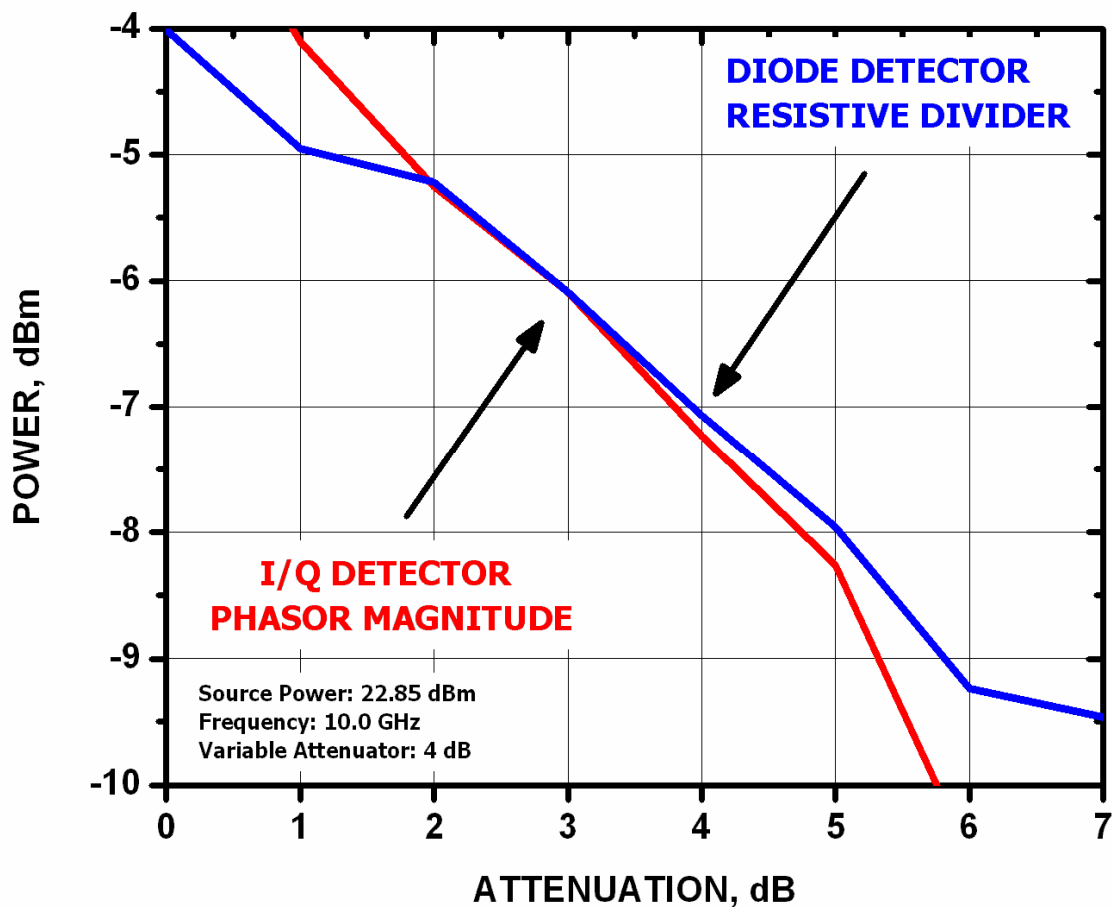

Figure A3. I/Q detector linearity.